Bulletin of the Seismological Society of America, Vol. 106, No. 5, pp. 2302–2312, October 2016, doi: 10.1785/0120160105

Nonlinear Suppression of High-Frequency *S* Waves by Strong Rayleigh Waves

by Norman H. Sleep and Nori Nakata

Abstract Strong Rayleigh waves are expected to bring the shallow subsurface into frictional failure. They may nonlinearly interact with high-frequency *S* waves. The widely applied Drucker and Prager (1952) rheology predicts that horizontal compression half-cycle of strong Rayleigh waves will increase the strength of the subsurface for *S* waves and predicts that *S* waves with dynamic accelerations $> 1g$ will reach the surface. We did not observe this effect. Rather, we observed that strong high-frequency *S* waves arrived at times of low Rayleigh-wave particle velocity. Physically, high-frequency *S* waves cause failure on horizontal fractures in which Rayleigh waves do not change the normal traction. Failure then may depend on the ratio of the shear invariant to the ambient vertical stress. The shear invariant is the square root of the sum of the squares of terms proportional to the resolved horizontal velocity from Rayleigh waves and to the resolved high-frequency dynamic acceleration from *S* waves. That is, an ellipse should bound resolved dynamic acceleration versus resolved particle velocity. Records from seven stations from the 2011 Tohoku earthquake and El Pedregal station during the 2015 Coquimbo Chilean earthquake exhibit this expected effect of this nonlinear interaction.

Introduction

Sufficiently strong seismic waves produce dynamic stresses that bring the shallow subsurface into frictional failure. Frictional sliding on cracks dissipates energy, nonlinearly attenuating the waves. The amplitude of the waves observed at the surface is thus less than it would be in a fully elastic medium. Different types of seismic waves interact nonlinearly, including *S* waves, *P* waves, surface waves, and near-field velocity pulses (Sleep and Nakata, 2015). These wave types may also interact with ambient deviatoric stresses. We restrict this article to nonlinear interaction of high-frequency *S* waves with Rayleigh waves.

Sleep and Nakata (2015) noted that strong Rayleigh waves appeared to suppress high-frequency *S* waves at station MYGH05 during the 2011 M_w 9.0 Great Tohoku earthquake. We discuss records from six additional stations that recorded strong *S* waves with coarrived strong Rayleigh waves during the Tohoku earthquake. Shear velocity well logs are available for all six stations. We also discuss the interaction of high-frequency *S* waves with low-frequency Rayleigh waves during the 16 September 2015 M_w 8.3 earthquake offshore of Coquimbo, Chile. This event produced both strong Rayleigh waves and strong *S* waves at El Pedregal, Chile (station code C1.CO03; 70.689° W, 30.839° S).

The purpose of this exercise is to appraise examples in which nonlinearity may have occurred in the shallow subsurface. Coarrival of strong *S* waves with strong Rayleigh waves is relatively rare; it does occur during major subduction ($\mathbf{M} > 8$) events with extensive source areas and long source durations. Our theory predicts that the effect is most likely at a site where the soil layer is thin or nonexistent. This phenomenon thus currently has only modest direct relevance to engineering site effects related to strong *S* waves. In particular, it would be foolhardy to assume that strong Rayleigh waves will arrive at just the right time to suppress strong *S* waves. Our intent is to compare theoretical predictions with data.

In general, our method requires high-frequency *S* waves with dynamic accelerations approaching $1g$ that impinge on a modern strong-motion station during long-period (~3 s) Rayleigh waves. It is preferable that strong *P* waves $\sim 1g$ (which affect normal traction on horizontal planes) do not impinge with the *S* waves, as additional nonlinear interaction is expected (Tobita *et al.*, 2010; Sleep and Nakata, 2015). For the Tohoku earthquake, we selected six stations with well logs where we have some information on subsurface geology. El Pedregal station recorded strong shaking during the 2015 Coquimbo Chilean earthquake, so we might exhibit the predicted effects of this nonlinear interaction. No other suitable records are available for this event. Subsurface structure has been measured for Chilean stations that recorded the great Maule earthquake (Molnar *et al.*, 2015); we examine two of these records. We did not find any other suitable records for other events.

Theory

We model nonlinear attenuation of seismic waves with the construct of frictional failure with forethought to our records. For *S* waves alone, failure occurs when the shear traction τ on a horizontal plane becomes greater than the failure traction τ_{fail}

$$\tau > \tau_{\text{fail}} = \mu(P_{\text{rock}} - P_{\text{water}}) \equiv \mu_{\text{eff}} \rho g z \approx \mu(\rho - \rho_w) g z, \quad (1)$$

in which μ is the coefficient of friction, ρ is the rock density, ρ_w is the water density, g is the acceleration of gravity, z is the depth, P_{water} is the fluid pressure, and P_{rock} is the rock pressure. The effective coefficient of friction μ_{eff} compacts notation. The approximate equality assumes that the water table is at the surface. Nonlinear attenuation occurs when dynamic stresses given by seismic waves exceed the failure criterion.

We make simplifying assumptions to generalize equation (1) for internal failure within a rock mass. First, we assume that the medium is isotropic. The seismic waves change the deviatoric stress tensor by $\Delta\tau_{ij}$ and the full stress tensor by $\Delta\sigma_{ij}$. In the near surface, *S* waves refract into nearly vertical paths where they produce shear traction on horizontal planes. Rayleigh waves and *S* waves do not change normal traction on those planes; it remains the effective lithostatic stress, $P_{\text{eff}} \equiv P_{\text{rock}} - P_{\text{water}}$ in the absence of strong *P* waves that also ascend in nearly vertical paths. Second, we assume that the shallow rock is pervasively cracked. Internal failure of the shallow rock depends on the shear-strain energy in the rock, which depends on the invariant of deviatoric stress $|\Delta\tau| \equiv \sqrt{0.5\Delta\tau_{ij}\Delta\tau_{ij}}$, which we define to give the shear traction in simple shear. The shear invariant for vertical *S* waves and Rayleigh waves is

$$|\Delta\tau|^2 = \Delta\tau_S^2 + \Delta\tau_R^2, \quad (2)$$

in which $\Delta\tau_S$ and $\Delta\tau_R$ are the changes in the deviatoric stresses associated with *S* waves and Rayleigh waves, respectively.

We apply well-known expressions for stresses in equation (2) in terms of observed acceleration and observed horizontal velocity, respectively, following Sleep and Nakata (2015). The free surface causes the shear traction associated with *S* waves to increase with depth downward to the quarter-wavelength depth. The shear traction on a shallow horizontal plane is $|\Delta\tau_S| = |\rho A_{\text{obs}} z|$, in which A_{obs} is the observed horizontal acceleration. Nonlinear failure occurs when the dynamic acceleration A normalized to the acceleration of gravity g exceeds the effective coefficient of friction. An implication is that the observed normalized acceleration A_{obs} remains less than the effective coefficient of friction:

$$\left|\frac{A_{\text{obs}}}{g}\right| < \mu_{\text{eff}}. \quad (3)$$

The criterion in equation (3) is only approximately correct for broadband signal in which the stresses at depth are not exactly related to the acceleration at the surface. Sleep and Nakata (2015) used the envelope function (the complex absolute value of the Hilbert transform) to decrease the phase dependence of plotted acceleration and to provide a better indication of the underground stress. Conveniently, this quantity varies much more slowly with time than do raw accelerations. We use the resolved envelope function, which is the square root of the sum of the squares of the two horizontal envelopes:

$$A_{\text{res}} \equiv \sqrt{A_{\text{NSenv}}^2 + A_{\text{EWenv}}^2}, \quad (4)$$

in which A_{NSenv} and A_{EWenv} are the north–south and east–west envelopes at each timestep, as our measure of observed acceleration.

The dynamic horizontal stress $\Delta\sigma_R$ from a Rayleigh wave is proportional to the horizontal ground velocity. The dynamic vertical stress is small near the free surface, so the dynamic deviatoric stress is $\Delta\tau_R = \Delta\sigma_R/2$. Thus,

$$\Delta\tau_R = \varepsilon\left[\frac{E}{(1-v^2)}\right] \approx \left[\frac{4}{3}\right] G\left[\frac{V_{\text{res}}}{c_{\text{Ray}}}\right], \quad (5)$$

in which $E = 2(1+v)G$ is the Young's modulus, G is the shear modulus, $\nu = \lambda/2(\lambda+G)$ is the Poisson's ratio, ε is the dynamic strain, λ is the second Lamé constant, c_{Ray} is the phase velocity of the Rayleigh wave, and the approximate equality assumes $\lambda = G$ (e.g., Turcotte and Schubert, 2002, p. 114). We also compute the resolved horizontal velocity at each timestep:

$$V_{\text{res}} \equiv \sqrt{V_{\text{NS}}^2 + V_{\text{EW}}^2}, \quad (6)$$

in which V_{NS} and V_{EW} are the north–south and east–west velocities to the particle velocity of the Rayleigh wave. The dynamic strain ε is $V_{\text{res}}/c_{\text{Ray}}$. As given in equation (6), invariant in equation (2) and the resolved velocity in equation (6) do not depend on the sign of the horizontal dynamic stress from the Rayleigh waves.

However, Rayleigh waves produce alternating dynamic horizontal compression and tension in the direction of propagation. They thus change the mean stress and the normal traction on vertical planes. It is attractive to apply Drucker and Prager (1952) plasticity with which Roten *et al.* (2014) modeled nonlinear seismic waves in Greater Los Angeles. Failure depends on $\mu_{\text{eff}} = |\Delta\tau|/|\sigma|$, in which $|\sigma| \equiv \sigma_{ii}/3$ is the mean stress including lithostatic pressure, compression positive. Modeling a Rayleigh wave as plane strain, the three principle stresses during the horizontal compression phase of the Rayleigh wave are P_{eff}, $P_{\text{eff}} + \Delta\sigma$, and $P_{\text{eff}} + \Delta\sigma/2$, and the mean stress is $|\sigma| = P_{\text{eff}} + \Delta\sigma/2$. The failure criterion is

$$\mu_{\text{eff}} = \frac{[\Delta\tau_S^2 + (\Delta\sigma_R/2)^2]^{1/2}}{P_{\text{eff}} + \Delta\sigma_R/2}. \quad (7)$$

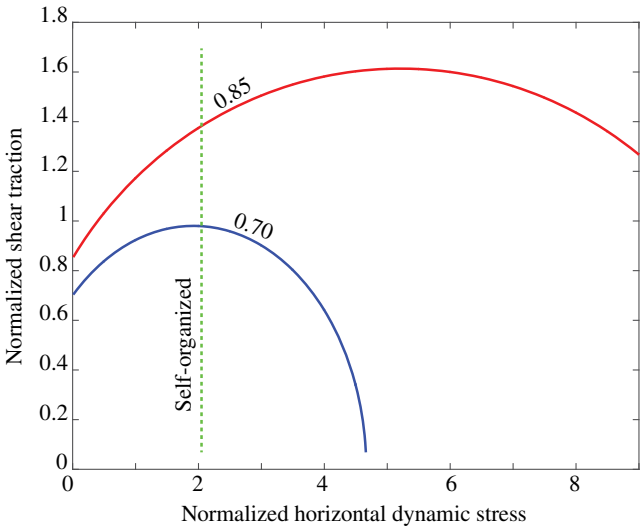

Figure 1. The shear traction and horizontal dynamic stresses are normalized to the effective stress for Drucker and Prager (1952) plasticity. We did not observe this behavior. Failure envelopes are shown for coefficients of friction of 0.70 and 0.85. For comparison, failure on optimal planes occurs with self-organized tectonic stress at a horizontal stress of 2.05 for $\mu = 0.80$. This stress is 2.31 for $\mu = 0.85$ and 1.71 for $\mu = 0.70$. The color version of this figure is available only in the electronic edition.

The predicted value of $\Delta\tau_S/P_{\text{eff}}$ is greater than μ_{eff} for moderately strong Rayleigh waves (Fig. 1). That is, S waves with accelerations $>1g$ are predicted to reach the surface during the horizontal compressional phase of Rayleigh waves for deep water table and hard rock, in which $\mu \approx 0.85$. We have no evidence of this situation actually occurring. We thus continue with the alternative predictions of horizontal stress for failure on optimally oriented faults. Failure occurs

$$\Delta\sigma_{\text{fail}} = \left[\frac{2\mu}{(1+\mu^2)^{1/2} \pm \mu}\right] P_{\text{eff}}, \tag{8}$$

in which $\Delta\sigma_{\text{fail}} = \Delta\sigma_T$ for horizontal tension with the plus sign and $\Delta\sigma_{\text{fail}} = \Delta\sigma_C$ for compression, and P_{eff} is the effective vertical stress. The full horizontal stresses at failure are $\sigma_{FT} \equiv P_{\text{eff}} - \Delta\sigma_T$ in tension and $\sigma_{FC} \equiv P_{\text{eff}} + \Delta\sigma_C$ in compression.

Sleep and Nakata (2015) did not resolve any directional effect for nonlinearity associated with Rayleigh waves during the Great Tohoku earthquake. If the effect really does not exist, one possibility is that the horizontal tectonic stress self-organizes when there is frequent nonlinearity during strong shaking in a thrust-fault environment. The ambient horizontal stress of $(\sigma_{FT} + \sigma_{FC})/2$ is furthest from failure during Rayleigh waves. The stress perturbation to cause failure is $\Delta\sigma_{\max} \equiv 2\mu(1+\mu^2)$ in all horizontal directions. If the actual horizontal stresses are distributed around this value, some favorably stressed cracks will fail when the dynamic stress is below $\Delta\sigma_{\max}$, but there will be no overall anisotropy with regard to Rayleigh-wave propagation directions and stress polarity.

Another effect occurs because normal traction on shallow horizontal planes (along which strong S waves cause failure) remains lithostatic. It is then unclear whether sudden changes in mean stress from Rayleigh waves affect failure during S waves. Formalisms are better developed for slip on a single fracture. The failure stress is $\tau_{\text{fail}} = \mu P_{\text{amb}} + \mu_\Delta \Delta P$, in which μ is the long-term coefficient of friction, P_{amb} is the ambient effective normal traction, and μ_Δ is the coefficient of friction for the incremental change in normal traction ΔP. The value of μ_Δ is much less than μ in rate and state friction (Linker and Dieterich, 1992; Perfettini *et al.*, 2001). An additional effect occurs below the water table. Dynamic compression (tension) of poorly drained compliant cracks causes the fluid pressure to increase above (decrease below) its steady-state macroscopic value. The local effective normal traction within the compressed (dilated) undrained crack increases (decreases) less than that within a drained crack (e.g., Wang *et al.*, 2014). This Skempton's coefficient effect causes μ_Δ to be less than μ by an unknown amount.

We present a formulation based on the normal traction on horizontal failure planes remaining constant. We retain the shear invariant in equation (2) to obtain

$$|\Delta\tau|^2 = \Delta\tau_S^2 + \Delta\tau_R^2 = A_{\text{obs}}^2 \rho^2 z^2 + C_1^2 V_{\text{res}}^2, \tag{9}$$

in which C_1 gathers the variables in equation (5). One would evaluate equation (9) near the quarter-wavelength depth for monochromatic S waves in which tractions on horizontal planes are the greatest. The equation applies qualitatively over a range of quarter-wavelength depths for the dominant frequency range of our broadband signal. There is effectively an unknown dimensionless factor in C_1 in equation (9). For failure in equation (9) from dynamic tension, the Coulomb ratio from equation (8) $\Delta\sigma_T/P_{\text{eff}}$ is 0.77. For reference, the value of $\Delta\sigma_{\max}$ for self-organized ambient stress is 2.05 and $\mu = 0.80$.

Simplification accrues by dividing both sides of equation (9) by the square of the failure stress $\tau_{\text{fail}} = \rho g \mu_{\text{eff}} z$:

$$\frac{|\Delta\tau|^2}{\tau_{\text{fail}}^2} = \frac{A_{\text{res}}^2}{A_{\text{fail}}^2} + \frac{V_{\text{res}}^2}{V_{\text{fail}}^2} < 1, \tag{10}$$

in which failure for S waves in the absence of Rayleigh waves occurs at the acceleration $A_{\text{fail}} \equiv \mu_{\text{eff}} g$ and shallow failure occurs from Rayleigh waves alone at the particle velocity V_{fail}. The inequality indicates that an ellipse from equation (10) bounds observed values of (A_{res}, V_{res}). Sleep and Nakata (2015) observed that the predicted ellipse in equation (10) bounds the (A_{res}, V_{res}) signal at MYGH05 station from the 2011 M_{w} 9.0 Great Tohoku earthquake. They only examined sites with borehole seismometers at depths >300 m. We present six other stations that may show this effect.

Application to the Great Tohoku Earthquake

There were six stations with S-wave velocity logs that recorded coarriving strong S waves and Rayleigh waves

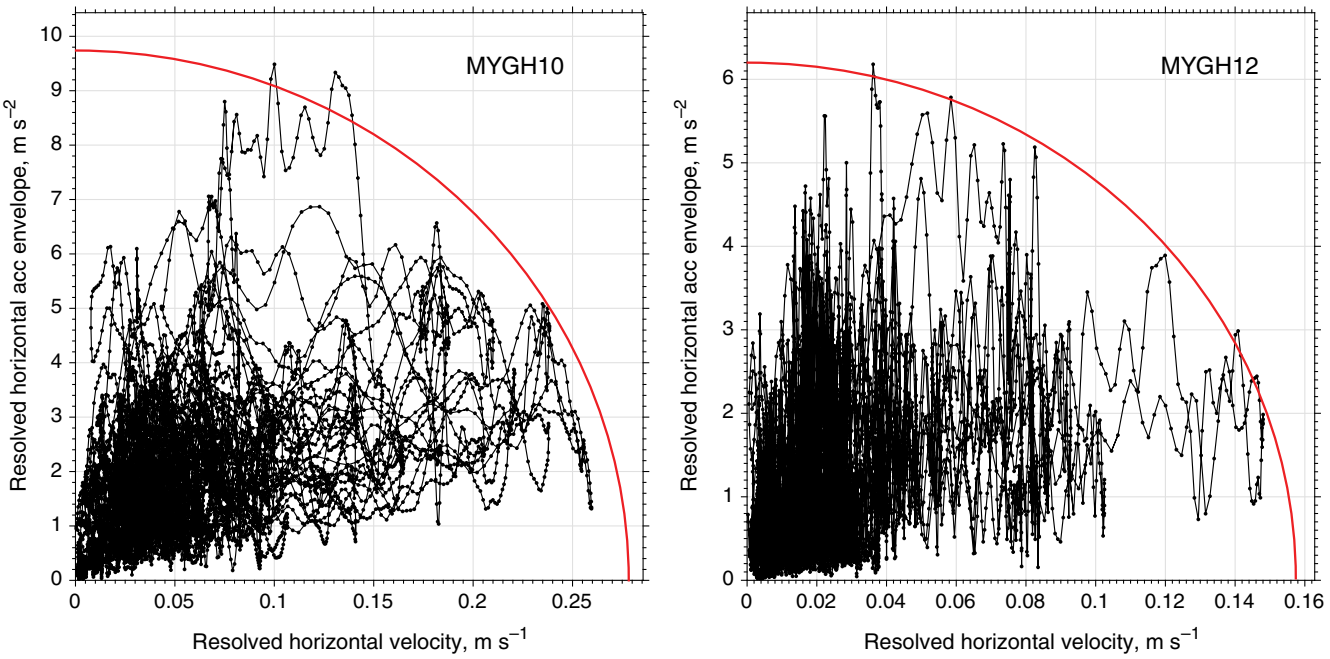

Figure 2. The resolved horizontal acceleration envelope from *S* waves is plotted as a function of the resolved horizontal velocity from Rayleigh waves for MYGH10 and MYGH12. An ellipse bounds the data as expected from equation (10). These stations had the strongest Rayleigh waves. The color version of this figure is available only in the electronic edition.

(Table 1) during the Great Tohoku earthquake. The surface receivers of KiK-net stations MYGH10 and MYGH12 recorded strong Rayleigh waves (Fig. 2). Stations FKSH08, FKSH09, MYGH03, and MYGH04 recorded moderate Rayleigh-wave amplitudes <0.12 m/s (Fig. 3). We show bounding ellipses by applying equation (10). Both A_{fail} and V_{fail} are effectively fitting parameters. There is a general tendency for high accelerations to occur at times of low Rayleigh-wave amplitude. We did not observe any very strong *S* waves during times of high Rayleigh-wave particle velocity that equation (7) predicts during the compressional half-cycle. Note that we did not attempt to distinguish compression from tensional half-cycles, many of the half-cycles were certainly compressional.

With regard to *S* waves at weak Rayleigh-wave amplitudes, the data show the expected effect of equation (3): that the maximum amplitude corresponding to the effective coefficient of friction is reached. The acceleration is expected

Table 1
Tohoku Stations

	Station					
	FSKH08	FSKH09	MYGH03	MYGH04	MYGH10	MYGH12
Latitude (° N)	37°16′45″	37°21′0″	37°55′8″	38°46′59″	37°56′17″	38°38′19″
Longitude (° E)	140°13′4″	140°25′47″	141°38′32″	141°19′44″	140°53′45″	141°26′46.5″
Elevation (m)	330	270	50	35	20	18
Age: Rock type	Q: Sandy gravel	Q: Sandy gravel	Q: Sandy gravel	MI: Fill dirt	Mud	Q: Sandy gravel
Depth (m)	0–8	0–10	0–4	0–4	0–3	0–6
S-wave velocity (m/s)	200–450	140–300	350	220	110–250	280
Age: Rock type	Q: Sandy gravel	Q: Welded tuff	P: Shale	P: Shale	N: Sand and gravel beds	Tr: Sandstone over shale
Depth (m)	8–48	10–44	4–32	4–36	3–34	6–34
S-wave velocity (m/s)	900	1930	700–1650	960–1840	390	870–1690
Maximum *S*-wave velocity (m/s)	1470	2540	2630	2830	770	2670
Depth (m)	Below 48	126–170	Below 32	Below 36	Below 114	Below 34
Deep failure particle velocity (m/s)	0.3011	0.2649	0.0628	0.0610	2.6075	0.0647

Data are provided by the National Research Institute for Earth Science and Disaster Prevention in Japan. *S*-wave velocities are given in piecewise-constant form. Tabulated lithological log boundaries do not necessarily correspond to tabulated *S*-wave velocity steps. Rock ages: MI, modern industrial; Q, Quaternary; N, Neogene; Tr, Triassic; P, Permian. Deep failure velocity for Rayleigh wave is computed at the top of the deep high-velocity layer; water table at the surface; phase velocity, 3000 m/s, coefficient of friction 0.8; rock density 2500 kg/m^3; self-organized tectonic stress.

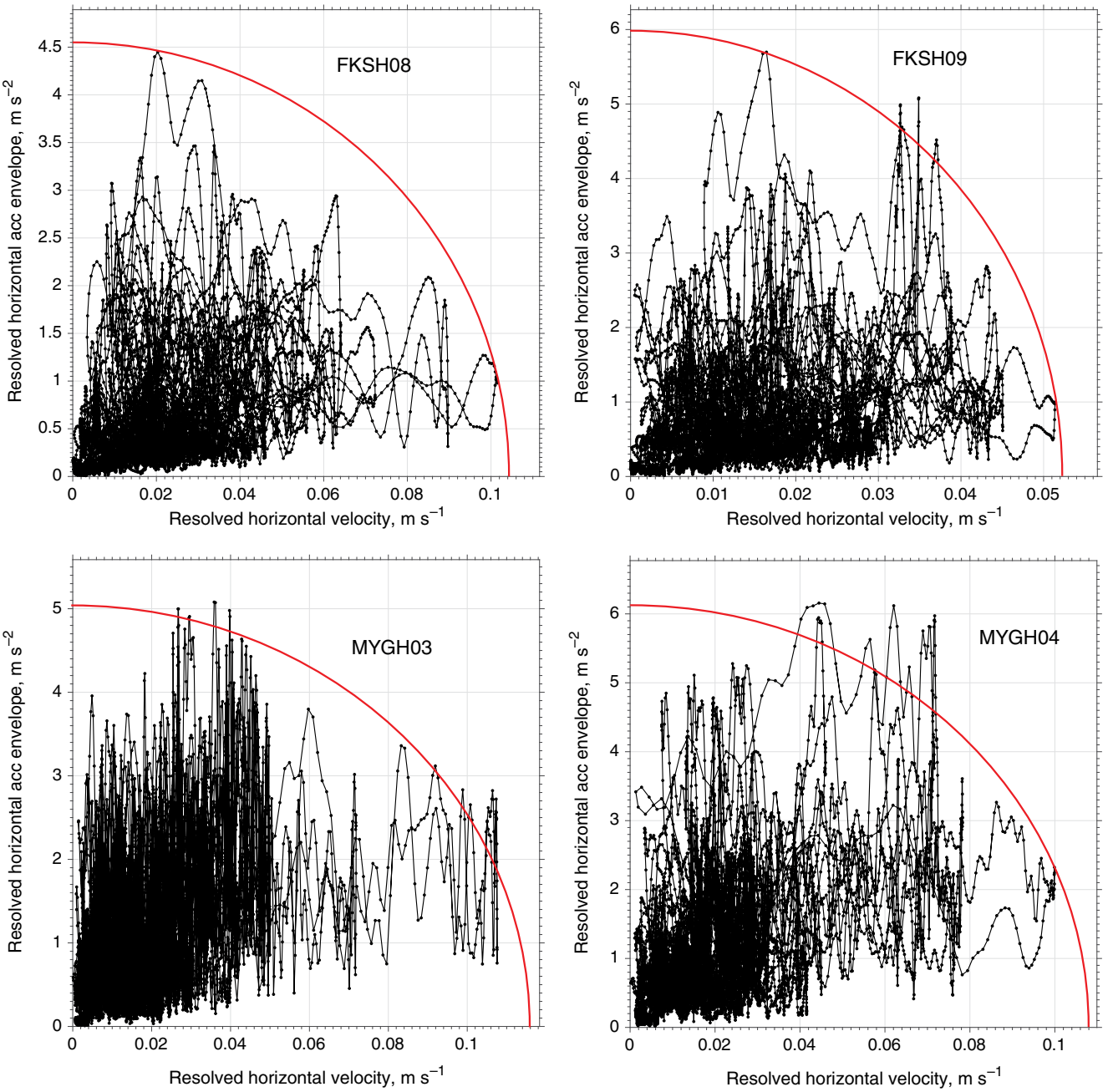

Figure 3. The resolved horizontal acceleration envelope from *S* waves is plotted as a function of the resolved horizontal velocity from Rayleigh waves for FKSH08, FKSH09, MYGH03, and MYGH04. An ellipse bounds the data as expected from equation (10). These stations had weaker Rayleigh waves than those in Figure 2. The color version of this figure is available only in the electronic edition.

to approach the maximum value multiple times if such clipping does, in fact, occur. Dynamic acceleration approached its maximum value multiple times at FKSH09, MYGH03, MYGH04 (Fig. 3), MYGH10, and MYGH12 (Fig. 2). There was only one excursion to its maximum with two peaks at FKSH08 (Fig. 3).

The intercept of the reference ellipse A_{fail} indicates the effective coefficient of friction in equation (3). It is 0.46, 0.60, 0.51, 0.61, 0.98, and 0.62 at FKSH08, FKSH09, MYGH03, MYGH04 (Fig. 3), MYGH10, and MYGH12 (Fig. 2), respectively. For comparison, the normalized intercept at station MYGH05 from the 2011 M_w 9.0 Great Tohoku earthquake is 0.48 (Sleep and Nakata, 2015).

We expect some variation in calculated μ_{eff} between stations. The laboratory coefficient of friction μ for shale ranges between 0.4 for clay-rich material and 0.85 for quartz-rich material (Kohli and Zoback, 2013). Shale with unknown clay content occurs beneath FSKH09, MYGH03, MYGH04, and MYGH12. The coefficient of friction for clay-poor hard rock is 0.85 (Byerlee, 1978). This value

may apply to sandy gravel beneath FKSH08, FKSH09, and MYGH10; welded tuff beneath FKSH09; and sandstone beneath MYGH12. We do not have data on water depth at our stations. The ratio of fluid pressure to rock pressure is about (1200 kg/m^3)/(2200 kg/m^3) = 0.55 for recent sediments and 1500/2500 = 0.6 for exhumed sediments and welded tuff. The maximum acceleration is expected to be $0.6 \times 0.85 = 0.51$ for the water table at the surface and hard rock and $0.55 \times 0.85 = 0.47$ for recent clay-poor sediments. The intercept for FKSH08 of 0.46 is slightly out of this range.

Only the acceleration intercept at MYGH10 of 0.98 is above the expected range. The site is above accumulating sediments with the uppermost 3 m being mud. It is conceivable that the shear modulus of the shallow mud decreased during strong shaking trapping *S* waves (Assimaki *et al.*, 2011).

Analysis of the velocity intercepts in Figures 2 and 3 is more complicated because we do not have precise data on the *S*-wave velocity from which to infer stiffness. The National Research Institute for Earth Science and Disaster Prevention in Japan provides *S*-wave velocities in piece-constant form. The tabulated velocity steps often do not correspond to tabulated changes in their lithology logs. That is, the velocity steps are often artifacts and velocity may often vary smoothly with depth. In addition, 3D structure is often important at KiK-net stations. Thompson *et al.* (2012) used published velocity logs and paired borehole and surface stations to classify low-amplitude linear response. Stations FKSH05, MYGH04, MYGH05, and MYGH10 have low interevent variability, but poor fits to 1D models. Stations MYGH03 and FKSH09 both had high interevent variability and poor fits to 1D models. Thompson *et al.* (2012) did not analyze MYGH12.

We can still appraise whether the recorded Rayleigh waves likely caused nonlinearity in the subsurface. Shallow stiff beds lie beneath MYGH03, MYGH04, and MYGH12. We calculated the particle velocity to cause failure using the generic phase velocity of 3 km/s for Japan (Nishida *et al.*, 2008). We assumed hard-rock material properties: rock density 2500 kg/m^3, coefficient of friction 0.8, and water table at the surface. We assumed failure where Coulomb ratio of $\Delta\sigma_{\max}$ for self-organized ambient stress is 2.05. The value for tensional failure $\Delta\sigma_T/P_{\text{eff}}$ is 0.77. The results may be rescaled for the value by dividing by 2.05/0.77 = 2.7. We give values for the top of the layer with the highest *S*-wave velocity (Table 1).

Stations MYGH03, MYGH04, and MYGH12 have shallow stiff rocks. The tabulated velocity for failure is ~0.06 m/s, which is well below the observed particle velocity. The actual failure velocity would be an additional factor of $\rho/(\rho - \rho_w) = \sim 1.7$ higher if the water table is deep. The intercepts are 0.12, 0.11, and 0.16, respectively. It is reasonable that the observed Rayleigh waves brought some depth interval of the hard rock into frictional failure.

Station FSKH09 has welded tuff between 10 and 44 m. The failure velocity for the tuff is 0.048–0.21 m/s over this interval with the same potential additional factor arising. The observed intercept is 0.06 m/s. It is conceivable that nonlinear failure from Rayleigh waves occurred within the tuff unit.

There are less stiff accumulating sediments at FSKH08 and MYGH10. Failure at the 8 m top of the gravel would occur at a particle velocity of 0.17 m/s and at 0.75 m/s within sand beneath MYGH10. The observed intercepts are 0.11 and 0.27 m/s. It is conceivable that Rayleigh waves caused very shallow nonlinear failure at these stations.

Intuitively, shallow failure might affect the frequency content of the *S* waves differently than deep failure. We apply this concept to stiff rock that is likely to fail in friction, that is, a larger fraction of a wavelength at high frequencies passes through a deep thick nonlinear zone than does a low-frequency wave and hence the high-frequency waves are suppressed more so than low-frequency waves. The sites with deep attenuation from Rayleigh waves are thus expected to show reduced high-frequency content at times of high Rayleigh-wave amplitude. To examine this topic, we compute spectra from the acceleration wavefields of the horizontal components. First, we compute the time-frequency spectrograms of acceleration in each component using *S* transform (Stockwell, 2007). Then, we average the resolved horizontal spectrograms over two time intervals in which the resolved velocities are high and low, respectively (thick and thin lines). We observe expected frequency at MYGH03, MYGH04, and MYGH12 where there is shallow, stiff rock (Fig. 4). The quarter-wavelength of the *S* waves provide a depth scale. The dominant frequency is crudely 10 Hz. The depth is 7.5 m for shallow material with *S*-wave velocity of 300 m/s. It is 40 and 70 m for velocities of 1600 and 2800 m/s.

We do not observe this frequency at the other stations (Fig. 5). We note that strong shaking may have decreased the shear modulus beneath these stations because *S*-wave energy is trapped within nonlinear sediments (Assimaki *et al.*, 2011). We do not attempt to quantitatively analyze out data for this effect. Kaklamanos *et al.* (2015) studied the nonlinear response of six KiK-net stations for the Tohoku earthquake. They did not study our stations because Thompson *et al.* (2012) showed that 1D models using the available well logs provided a poor fit to low-amplitude linear data.

Application to El Pedregal Station in Chile

We present another possible example from Chile. Among Chilean stations operated during the 2015 M_w 8.3 earthquake offshore of Coquimbo, only El Pedregal station recorded *S*-wave and Rayleigh-wave amplitudes that were large enough to examine the predictions of equation (10). This station is about 90 km northeast from the epicenter and recorded the strongest ground motion among available stations.

Subsurface properties are not available for El Pedregal. We infer them crudely from the interactive satellite photo and map provided by the Center for Engineering Strong-Motion Data (CESMD). The station rests upon cultivated land on an

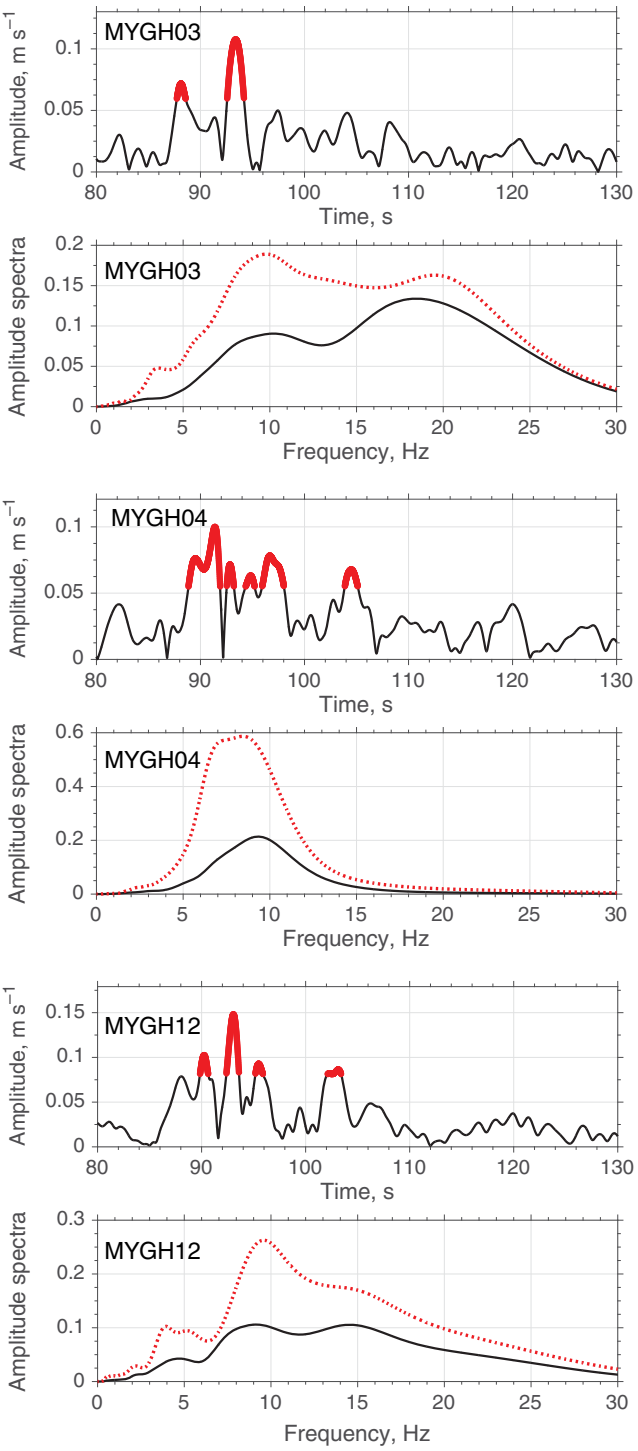

Figure 4. The resolved horizontal particle velocity for hard rock stations is plotted as a function of time after the start of the Tohoku earthquake. Spectra are obtained from times of weaker amplitude (thin lines) and high amplitude (thick lines). The high frequencies in the spectra at times of high amplitude (dashed lines) are decreased relative spectra at times of low amplitude (solid lines). The color version of this figure is available only in the electronic edition.

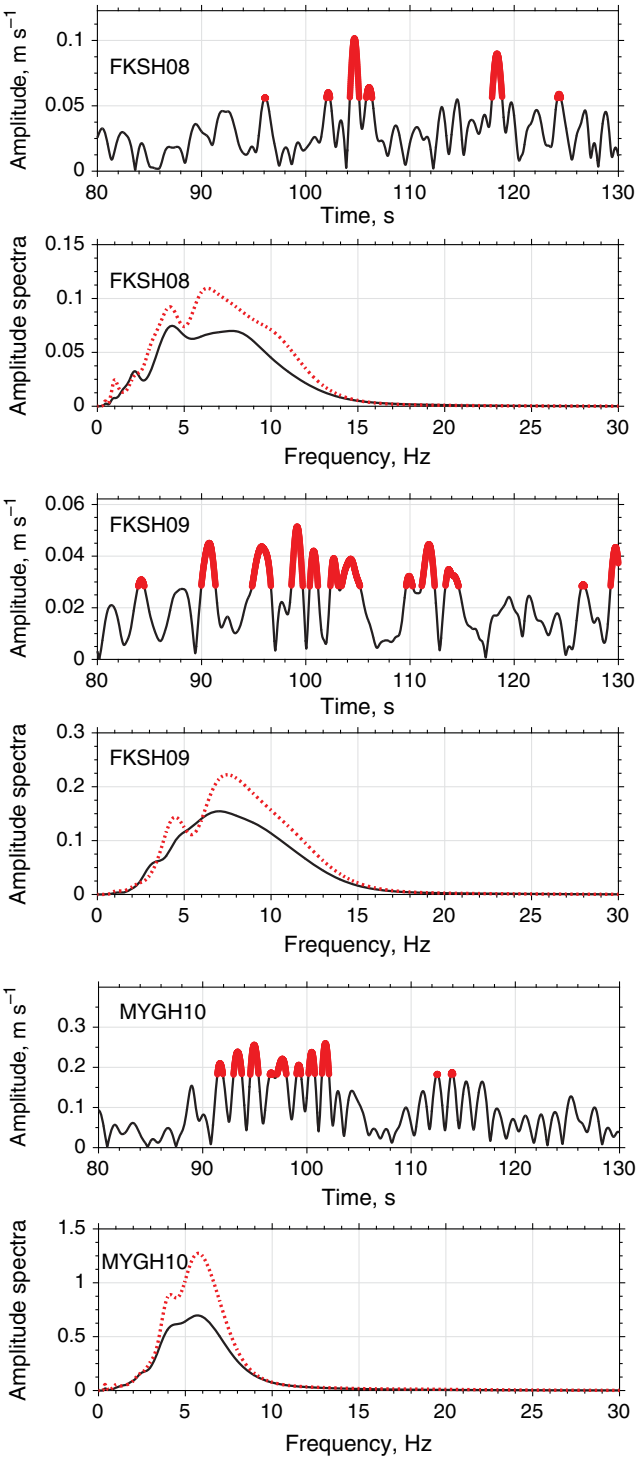

Figure 5. Amplitudes of the resolved particle velocity and spectra for accumulating sediment stations, plotted as in Figure 4. The spectral peak moves toward high frequencies. The color version of this figure is available only in the electronic edition.

incised river terrace at the confluence of a tributary with El Rio Mostazal. Coarse river gravel likely overlie exhumed hydrothermally altered hard rock of the volcanic Viñita formation (Mpodozis and Cornejo, 1988). The Google Earth photo linked to the CESMD website (see Data and Resources) indicates that the station is within 10 m of a small (unfarmed) outcrop of hard rock that is not resolved on the geological map of Mpodozis and Cornejo (1988). The El Pedregal site

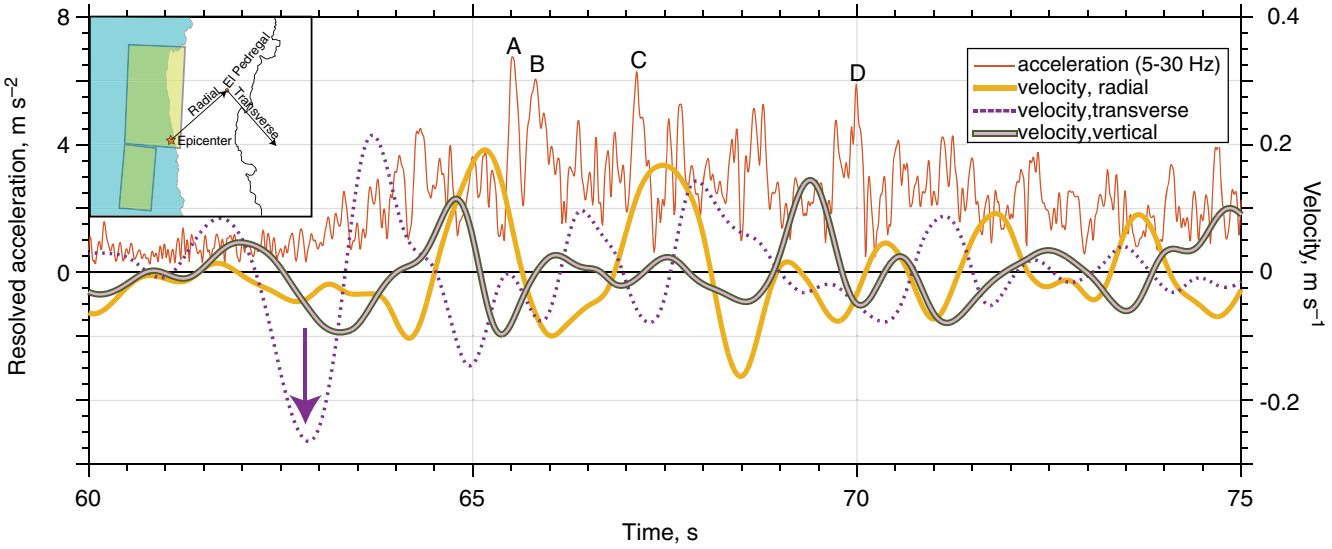

Figure 6. The observed resolved acceleration envelope (thin solid line) represents high-frequency *S* waves as a function of time (time 0 s is the origin time of the earthquake on the catalog). Four acceleration peaks with similar amplitudes (A–D) occur, as expected from equation (3). The low-frequency components are vertical, tracked line; transverse relative to the epicenter, dashed line; and radial, thick solid line. However, the finite-fault area (inset) is broad enough that transverse signal is likely mostly Rayleigh waves that originated away from the epicenter. The acceleration peaks occurred at times of low particle velocity as expected from equation (10). However, the strongest velocity peak (arrow) may have occurred before the onset of strong *S* waves. Seismic data and map are from the Center for Engineering Strong-Motion Data (CESMD). The color version of this figure is available only in the electronic edition.

thus may be similar to MYGH05 where 2 m of gravel overlies exhumed rock. We thus assume that the El Pedregal site behaved like fractured rock rather than like clay-rich soil.

With regard to hydrology, the gravels and the weathered shallow exhumed rock are likely well drained. The terrace is ~10 m above present river level. The water table is likely about that deep. The signal of the event is broadband so there is no well-defined quarter-wavelength depth. The dominant period of the *S* waves on an acceleration seismogram is crudely 0.1 s (provided by CESMD) as at MYGH05. We do not have subsurface velocity information for El Pedregal. For a generic shallow *S*-wave velocity of 400 m/s for gravel, the quarter-wavelength depth is ~10 m. It is ~70 m for hard rock with a velocity of 2800 m/s.

We again separate Rayleigh waves from high-frequency *S* waves with band-pass filters, retaining 0.1–1 Hz and 5–30 Hz, respectively. Strong signal arrived over an ~15 s interval (Fig. 6). El Pedregal is close to the finite area of fault slip (Fig. 6). The radial and transverse components relative to the epicenter do not provide a good criterion for distinguishing Rayleigh waves from Love waves. The vertical component is out of phase with the horizontal components as expected for Rayleigh waves. This dip-slip event is expected to produce stronger Rayleigh waves than Love waves.

Nonlinear attenuation from equation (3) should clip *S* waves at a normalized acceleration equivalent to the effective coefficient of friction in equation (3). One expects multiple peaks of similar amplitude. The record shows four such peaks (marked as A–D in Fig. 6). These peaks occur at times of low Rayleigh particle velocity.

An ellipse bounds the signal as predicted by equation (10) in Figure 7. The normalized acceleration intercept in equation (3) of ~7 m/s^2 corresponds to an effective coefficient of friction of 0.7. The inferred effective coefficient of friction beneath El Pedregal is acceptable for clay-poor gravels and exhumed hard rock partly above the water table.

As a caveat, we do not have information independent of the seismogram (Fig. 6) on the timing and spatial distribution of the sources of impinging strong high-frequency *S* waves. In particular, the strongest low-frequency signal (Fig. 6, arrow) arrived before any recorded strong *S*-wave pulses. It is conceivable that the Rayleigh wave suppressed the *S* waves. It is also conceivable that no strong *S* wave arrived until after that time.

The velocity intercept is 0.18 m/s (Fig. 7). We do not know the site parameters for applying equations (5) and (8). That is, we would need the phase velocity of Rayleigh waves, the quarter-wavelength depth of *S* waves, and the stiffness *G* at depth in equation (5). For plausibility, our intercept is similar to 0.215 m/s from MYGH05 and 0.16 m/s for MYGH12 for the Great Tohoku earthquake.

Application to Maule Earthquake in Chile

The 2010 M_w 8.8 Maule earthquake produced strong seismic waves at Angol station (ANGO, 37.80° S, 72.71° W) and Concepción (CCSP, 36.84° S, 73.11° W). We discuss records for completeness and for caveat on accumulating clay-rich sediments.

Boroschek *et al.* (2012) and Molnar *et al.* (2015) obtained the *S*-wave velocity from reliable shallow well log

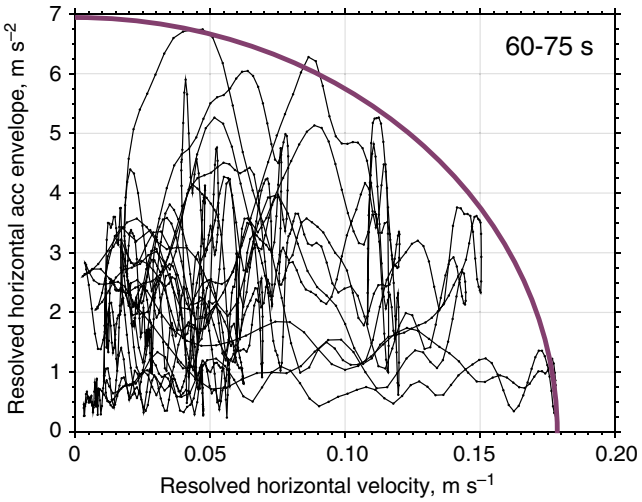

Figure 7. The resolved horizontal acceleration envelope from *S* waves as a function of the resolved horizontal velocity from Rayleigh waves at El Pedregal. An ellipse bounds the data as expected from equation (10). Seismic data are from the CESMD. The color version of this figure is available only in the electronic edition.

and surface seismic data. They provide lithology logs: 4.5 m of silty sand and 21 m of clay-cover-fractured metamorphic rock at CCSP. The uppermost 13.5 m at ANGO are clay and silty sand. Gravel, volcanic tuff, breccia, and bouldery gravel underlie these accumulating sediments. The water table at ANGO and CCSP was 2.80 and 1.00 m, respectively. We analyze the velocity and acceleration as we did in the previous sections (Fig. 8).

The strongest acceleration pulses arrived at times of modest particle velocity at both stations. However, only one incident of strong acceleration occurred at each station. These excursions inadequately constrain upper intercepts of the bounding ellipses. In addition, the peak accelerations of 0.85 and 0.51g at ANGO and CCSP are higher than expected of frictional failure criteria ($<0.4g$) of clay-rich rock with shallow a water table. Rather, ductile failure of the clay-rich sediments may have trapped *S* waves (Assimaki *et al.*, 2011). With regard to ductility, Boroschek *et al.* (2012) note the presence of low-plasticity clays at both ARGO and CCSP. They distinguish between the water table depth and depth ranges below the water table in which saturated groundwater affects *P*-wave velocity within clay-rich sediment. They state that the effect occurs below 13.50 m at ARGO and 4.50 m at CCSP rather than at the shallow water table itself.

Stiffer rock underlies the shallow sediments at both stations. We compute the failure velocity for Rayleigh waves retaining the parameters used in Table 1. Material with *S*-wave velocity of 800 m/s lies below 18 m at ANGO. Metamorphic rock with an *S*-wave velocity of 1600 m/s underlies CCSP below 59 m. The computed failure velocities for self-organized horizontal stress are 0.38 and 0.31 m/s. These velocities are comparable to the observed velocity intercepts of 0.27 and 0.43 m/s. The occurrence of frictional failure within the uppermost stiff rocks is reasonable. We have little evidence of such failure suppressing *S* waves at these stations.

We examined the records for changes in spectral content (Fig. 9). It moved toward higher frequencies at CCSP as it did

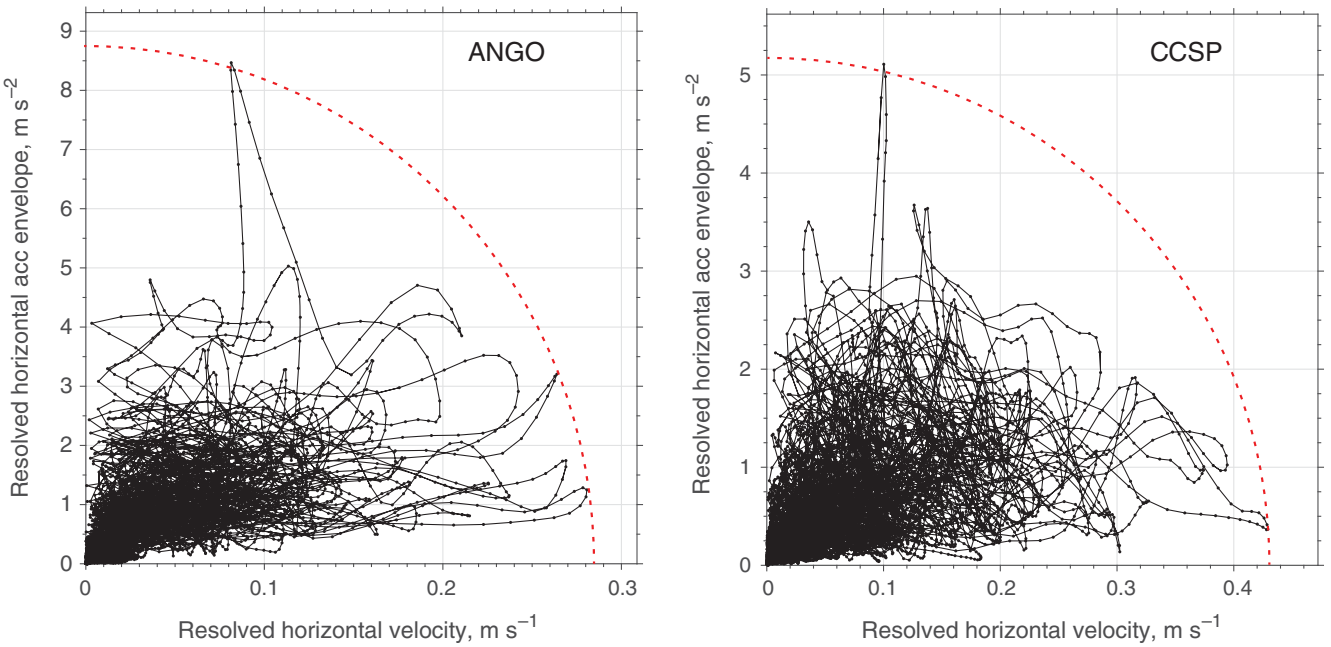

Figure 8. The resolved horizontal acceleration envelope from *S* waves as a function of the resolved horizontal velocity from Rayleigh waves at Angol station (ANGO) and Concepción (CCSP) for the Maule earthquakes. A single incidence of high-dynamic acceleration defines the upper intercept of the bounding ellipse (dashed) from equation (10). Seismic data are from the CESMD. The color version of this figure is available only in the electronic edition.

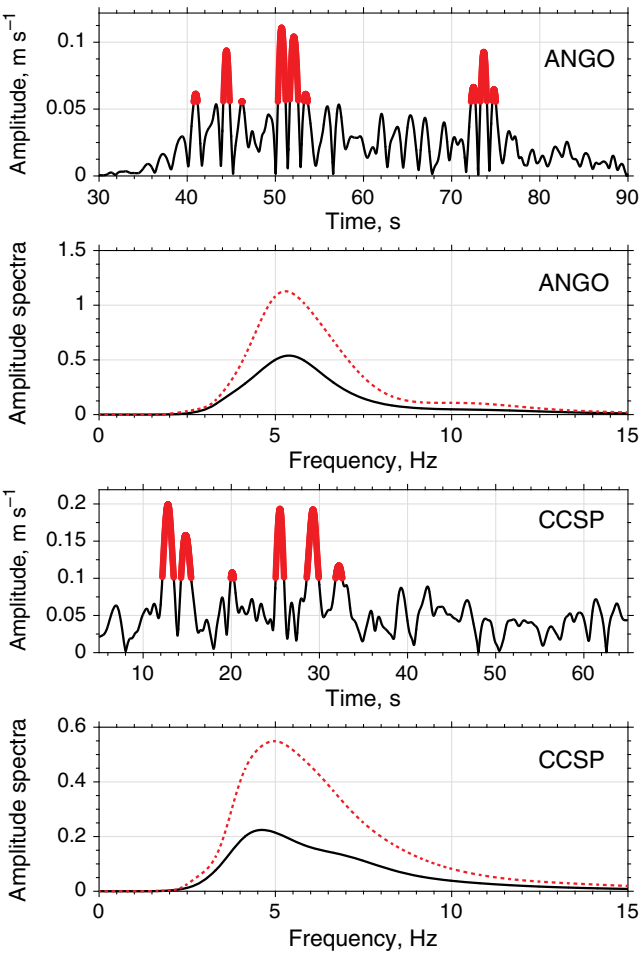

Figure 9. Amplitudes of the resolved particle velocity and spectra for ANGO and CCSP plotted as in Figure 4. Significant accumulating sediments lie beneath both stations. The spectral peak moves toward high frequencies at CCSP and changes little at ANGO. The color version of this figure is available only in the electronic edition.

with the Tohoku stations at accumulating sediment sites in Figure 5. However, the spectra peak changed little at ANGO.

Discussion and Conclusions

We observe a general tendency for strong high-frequency *S* waves to arrive during times of weak Rayleigh-wave particle velocity. We do not see strong *S* waves as expected from the Drucker and Prager (1952) failure criterion in equation (7) at times of strong Rayleigh waves. We noted that vertically propagating *S* wave should produce failure on horizontal planes. Rayleigh waves do not change the normal traction on these planes. We proposed an alternative failure criterion in equation (9) for which the normal traction on horizontal planes remains constant. The criterion retains the feature of a rock that has become nonlinear from Rayleigh waves will also be nonlinear for *S* waves. A prediction of this theory in equation (10) is that an ellipse bounds resolved acceleration versus resolved horizontal velocity. We observed this effect for six additional stations for the Tohoku earthquake and El Pedregal Station for the offshore Coquimbo earthquake. Data from two stations for the Maule record are compatible with hypothesis. Dynamic accelerations normalized to the acceleration of gravity are bounded by acceptable effective coefficients of friction in equation (3).

We do not have enough information on the subsurface velocity structure to appraise the implications for the velocity intercepts in Figures 2, 3, and 7. Shallow stiff-exhumed rock lies beneath MYGH03, MYGH04, MYGH05 (examined by Sleep and Nakata, 2015), MYGH12, and likely El Pedregal. It is likely that the observed Rayleigh waves caused nonlinear failure in the uppermost hard rock. It is conceivable that nonlinear behavior occurred with the uppermost 10 m of accumulating sediments at the other stations.

We noted that high frequencies were preferentially suppressed at the three Tohoku hard rock stations but not at the accumulating sediment stations. There are too few records to draw conclusions from this observation. The effect should be looked at as other records become available. Dense subsurface arrays with high-resolution logs would help greatly.

It might be possible to use many stations as an array to disentangle Rayleigh waves from Love waves. It is not clear if the station coverage for Tohoku is sufficient. A successful implementation would allow computation of dynamic stress and strain in the shallow subsurface. In addition, nonlinear attenuation will occur at places of random constructive interference of numerous waves. Nonlinear attenuation at these places is a virtual source of moment release, that is, a sink that decreases seismic-wave energy. The site will radiate seismic waves. Knowledge of the low-amplitude seismic structure of the region would certainly help with the massive analysis. There is a related sampling bias of *S*-wave suppression. Very strong Rayleigh waves and Love waves that bring the uppermost few hundred meters into nonlinear frictional failure will not propagate (Roten *et al.*, 2014). One is unlikely to have a station at the rare places where focusing and constructive interference lead to very strong surface waves that would greatly suppress *S* waves.

With regard to frictional rheology, Drucker and Prager (1952) plasticity provides predictions of very strong high-frequency *S* waves that we did not observe. We note that this rheology also conflicts with models for noninteracting cracks when one of the principal stresses approaches absolute tension (Jana and Chatterjee, 2013). The occurrence of stress concentrations with local absolute tension in the shallow subsurface during shaking and the maintenance of the vertical stress on horizontal planes by the free surface conceivably may make Drucker and Prager (1952) plasticity inapplicable for strong high-frequency *S* waves in this case. Numerical calculations with pervasive interacting cracks would be onerous. Observation of the interaction of *S* waves and Rayleigh waves by a dense borehole array would be revealing. High-resolution well logs would be quite helpful.

There are still too few data to apply formal statistics. We present a qualm related to FSKH08 in which the Rayleigh waves were relatively weak. That is, a bounding ellipse

might result even when Rayleigh waves and *S* waves are random uncorrelated time series. It is somewhat unlikely that the highest values of both time series would occur at the same time. The presence of multiple incidences to high accelerations and high-particle velocities provides some checking. There were only single high-acceleration incidents for each of the Maule records (Fig. 9) so this check was not available. Simple calculations are available as to whether frictional failure from Rayleigh waves should have occurred.

Data and Resources

Japanese seismograms and subsurface station information are publicly available from the National Research Institute for Earth Science and Disaster Prevention in Japan. The seismic data, maps, spectra, and satellite photos for El Pedregal station are publicly available from the Center for Engineering Strong-Motion Data (CESMD) and their link to Google Earth (http://www.google.com/earth/, last accessed July 2016). Maule data are available from CESMD. The rest of the data used in this article came from published sources listed in the references.

Acknowledgments

We would like to thank Rubén Boroschek for promptly answering the questions on subsurface structure beneath El Pedregal station. We also thank two anonymous reviewers for the suggestion to examine Japanese records in addition to the Chilean ones and for providing helpful comments. This research was supported by the Southern California Earthquake Center (SCEC). SCEC is funded by National Science foundation (NSF) Cooperative Agreement EAR-0106924 and U.S. Geological Survey Cooperative Agreement 02HQAG0008. The SCEC Contribution Number for this article is 6298.

References

Assimaki, D., W. Li, and A. Kalos (2011). A wavelet-based seismogram inversion algorithm for the in situ characterization of nonlinear soil behavior, *Pure Appl. Geophys.* **168,** 1669–1691, doi: 10.1007/s00024-010-0198-6.

Boroschek, R. L., U. F. Yáñez, B. I. Bejarano, S. Molnar, and G. A. Torres (2012). Caracterizacion geotecnica estaciones de acelerografos de la Universidad de Chile, *Report of FCFM (Facultad de Ciencias Físicas y Matemáticas) and IDIEM*, Universidad de Chile, Santiago, 587 pp.

Byerlee, J. (1978). Friction in rocks, *Pure Appl. Geophys.* **116,** 616–626.

Drucker, D. C., and W. Prager (1952). Soil mechanics and plastic analysis or limit design, *Q. Appl. Math.* **10,** 157–165.

Jana, P., and A. Chatterjee (2013). Modal damping in vibrating objects via dissipation from dispersed frictional microcracks, *Proc. Math. Phys. Sci.* **469,** doi: 10.1098/rspa.2012.0685.

Kaklamanos, J., L. G. Baise, E. M. Thompson, and L. Dorfmann (2015). Comparison of 1D linear, equivalent-linear, and nonlinear site response models at six KiK-net validation sites, *Soil Dynam. Earthq. Eng.* **69,** 207–219.

Kohli, A. H., and M. D. Zoback (2013). Frictional properties of shale reservoir rocks, *J. Geophys. Res.* **118,** 5109–5125, doi: 10.1002/jgrb.50346.

Linker, M. F., and J. H. Dieterich (1992). Effects of variable normal stress on rock friction: Observations and constitutive equations, *J. Geophys. Res.* **97,** 4923–4940.

Molnar, S., C. E. Ventura, R. Boroschek, and M. Archila (2015). Site characterization at Chilean strong-motion stations: Comparison of downhole and microtremor shear-wave velocity methods, *Soil Dynam. Earthq. Eng.* **79,** 22–35.

Mpodozis, M. C., and P. Cornejo (1988). Hoja Piscoi Elqui IV region de Coquimbo, *Carta Geologica de Chile, No. 68*. Servivo Geologica de Chile, Santiago, Chile, 164 pp., scale 1:250,000.

Nishida, K., H. Kawakatsu, and K. Obara (2008). Three-dimensional crustal *S* wave velocity structure in Japan using microseismic data recorded by Hi-net tiltmeters, *J. Geophys. Res.* **113,** no. B10302, doi: 10.1029/2007JB005395.

Perfettini, H., J. Schmittbuhl, J. R. Rice, and M. Cocco (2001). Frictional response induced by time-dependent fluctuations of the normal load, *J. Geophys. Res.* **106,** no. B7, 13,455–13,472.

Roten, D., K. B. Olsen, S. Day, Y. Cui, and D. Fäh (2014). Expected seismic shaking in Los Angeles reduced by San Andreas Fault zone plasticity, *Geophys. Res. Lett.* **41,** 2769–2777, doi: 10.1002/2014GL059411.

Sleep, N. H., and N. Nakata (2015). Nonlinear attenuation from the interaction between different types of seismic waves and interaction of seismic waves with shallow ambient tectonic stress, *Geochem. Geophys. Geosyst.* **16,** 2336–2363, doi: 10.1002/2015GC005832.

Stockwell, R. G. (2007). A basis for efficient representation of the S-transform, *Digit. Signal. Process.* **17,** 371–393.

Thompson, E. M., L. G. Baise, Y. Tanaka, and R. E. Kayen (2012). A taxonomy of site response complexity, *Soil Dynam. Earthq. Eng.* **41,** 32–43.

Tobita, T., S. Iai, and T. Iwata (2010). Numerical analysis of near-field asymmetric vertical motion, *Bull. Seismol. Soc. Am.* **100,** no. 4, 1456–1469.

Turcotte, D. L., and G. Schubert (2002). *Geodynamics*, Second Ed., John Wiley, New York, 456 pp.

Wang, J., C. Xu, J. T. Freymueller, Z. Li, and W. Shen (2014). Sensitivity of Coulomb stress change to the parameters of the Coulomb failure model: A case study using the 2008 M_w 7.9 Wenchuan earthquake, *J. Geophys. Res.* **119,** 3371–3392, doi: 10.1002/2012JB009860.

Department of Geophysics
Stanford University
397 Panama Mall
Stanford, California 94305
norm@stanford.edu

Manuscript received 5 April 2016;
Published Online 16 August 2016